JKAS
Journal of the Korean Astronomical Society
http://jkas.kas.org
eISSN: 2288-890X · pISSN: 1225-4614
JKAS (2023), **56**, 1, 23–33
doi: 10.5303/JKAS.2023.56.1.23

A Monte Carlo Study of the Diffusion Process of Thomson-Scattered Line Radiation in Phase Space

Hyeon Yong Choe and Hee-Won Lee*

Department of Physics and Astronomy, Sejong University, 209, Neungdong-ro, Gwangjin-gu, Seoul, Republic of Korea
*Corresponding Author: H.-W. Lee, hwlee@sejong.ac.kr

Received February 2, 2023; Accepted March 1, 2023; Published March 10, 2023

Abstract

We investigate the diffusion process of Thomson-scattered line photons in both real space and frequency space through a Monte Carlo approach. The emission source is assumed to be monochromatic and point-like embedded at the center of a free electron region in the form of a sphere and a slab. In the case of a spherical region, the line profiles emergent at a location of Thomson optical depth $\tau_{\rm Th}$ from the source exhibit the full width of the half maximum $\sigma_\lambda \simeq \tau_{\rm Th}^{1.5}$. In the slab case, we focus on the polarization behavior where the polarization direction flips from the normal direction of the slab to the parallel as the slab optical depth $\tau_{\rm Th}$ increases from $\tau_{\rm Th} \ll 1$ to $\tau_{\rm Th} \gg 1$. We propose that the polarization flip to the parallel direction to the slab surface in optically thick slabs is attributed to the robustness of the Stokes parameter Q along the vertical axis with respect to the observer's line of sight whereas randomization dominates the remaining region as $\tau_{\rm Th}$ increases. A brief discussion on the importance of our study is presented.

Keywords: radiative transfer — scattering — polarization

1. Introduction

Various spectral emission lines are formed in ionized nebulae through recombination or collisional excitation followed by radiative de-excitation. These emission nebulae are an essential aspect of astrophysically important objects including active galactic nuclei, x-ray binaries, cataclysmic variables, planetary nebulae, symbiotic stars and remnants of various explosive events such as supernovae and gamma ray bursts. Emission lines carry important information regarding the chemical abundance, kinematics and matter distribution (e.g., Osterbrock 1989; Warner 1995).

These emission lines are formed in an environment where free electrons are prevalent so that electron scattering is also an essential ingredient that has to be incorporated in the investigation of the emission line radiative transfer. UV and optical emission lines are very efficient coolants for a photoionized nebula, so that the nebula is maintained in thermal equilibrium with a temperature $\sim 10^4$ K. The thermal speed of free electrons corresponding to this temperature is ~ 400 km s^{-1}, from which emission line photons acquire a Doppler factor $\Delta\lambda/\lambda \sim 1.3 \times 10^{-3}$ per each electron scattering event. This implies that Thomson scattering of emission line photons give rise to the formation of broad wing features whose strength and width are determined by the scattering optical depth and the electron temperature. In addition, the cross section of Thomson scattering is constant so that the line photons may escape from the scattering region through a random-walk like fashion when the Thomson scattering optical depth is high.

Chandrasekhar (1960) investigated radiative transfer of Thomson-scattered radiation in a slab geometry to show that emergent radiation can be linearly polarized with the degree up to 11.7 percent when the slab is sufficiently optically thick with respect to Thomson scattering. Dependent on the Thomson optical depth, the polarization behaviors are quite complicated, rendering linear polarimetry an important probe to study the accretion disk in these objects (e.g., Agol & Blaes 1996; Afanasiev et al. 2019). Angel (1969) investigated the polarization of Thomson-scattered radiation in oblate spheroidal free electron regions adopting a Monte Carlo technique. He verified the limiting value of 11.7 percent is achieved in a slab-like geometry as the Thomson optical depth becomes sufficiently high.

Phillips & Meszaros (1986) investigated the linear polarization of Thomson-scattered radiation in slab geometries. They found that linear polarization develops along the normal direction to the slab when the slab is optically thin. However, the polarization direction flips to the parallel direction and the linear degree of polarization approaches 11.7 percent as the Thomson optical depth increases. However, these studies are

limited to the properties of the integrated radiation disregarding the diffusion nature that takes place in both real space and frequency spaces.

Lee (1999) pointed out that polarization of an emission line emergent from a Thomson scattering medium can differ as a function of wavelength because profile broadening is coupled to the scattering number, which, in turn, affects the linear degree of polarization. Using a Monte Carlo method, Kim et al. (2007) demonstrated the possibility that Thomson-scattered line features may exhibit complicated polarization structures despite the wavelength independence of the Thomson scattering cross section. Further complications can be expected for Thomson scattered spectral lines because the scattering number may affect the surface brightness, profile broadening and polarization simultaneously.

With the advent of integral field spectrographs, spectroscopic and imaging observations can be achieved in a very efficient way, which necessitates the investigation of photon diffusion processes in both real and frequency spaces. In this paper, we carry out Monte Carlo simulations to investigate the basic properties of the diffusion processes adopting spherical regions and slab regions with uniform electron density.

2. Frequency Redistribution

2.1. Monte Carlo Procedure

The Thomson scattering cross section is the basic physical quantity which is given by the well-known formula

$$\sigma_{\rm Th} = \frac{8\pi}{3} r_e^2, \tag{1}$$

where $r_e = e^2/m_e c^2$ is the classical electron radius. Here, m_e and c are the electron mass and speed of light and $e = 4.854 \times 10^{-10}$ esu is the electric charge given in c.g.s. unit.

In this section, we describe our Monte Carlo code for simulating the transfer of line photons that are Thomson-scattered in an ionized region. The scattering region is assumed to be a sphere or a slab, where a line emitting point source is embedded at the center and free electrons are uniformly distributed inside the region.

The line emitting source being assumed to be isotropic, and the simulation begins with the generation of an initial photon at the central point source. We trace the photon step by step in scattering processes, and collect the information of each photons for the line-of-sight. In the simulation, we trace each photon from generation until it escapes from the scattering region and reaches the detector. We assume that the line emitting source is purely monochromatic and isotropic.

The free path length l between scattering events is related to the scattering optical depth τ by

$$\tau = n_e \sigma_{\rm Th} l \tag{2}$$

where n_e is the electron number density inside the scattering region.

The wavelength independence of the Thomson scattering cross section guarantees that the Thomson scattering optical depth is directly proportional to the physical path length between scattering events. Therefore, one is allowed to make a direct use of τ to locate the physical location of each photon while we trace it in the simulation. In this case, the scattering region is specified by the total Thomson optical depth $\tau_{\rm tot}$ defined by

$$\tau_{\rm tot} = n_e \sigma_{\rm Th} R, \tag{3}$$

where R is the radius of the sphere or the thickness of the slab.

The scattering optical depth between scattering events is chosen in a probabilistic way. We note that the probability that Thomson scattering occurs within a scattering optical depth τ is

$$P(\tau) = \int_0^\tau e^{-x} dx = 1 - e^{-\tau}. \tag{4}$$

We choose a number r using a uniform random number generator in the interval $[0, 1]$ to identify it with $P(\tau)$, which should also be in the same interval. Equation (4) is readily inverted to yield

$$\tau = \ln\left[1 - P(\tau)\right] = \ln(1 - r). \tag{5}$$

Noting that $1 - r$ is also regarded as a uniform random number in the interval $[0, 1]$, we simply put

$$\tau = \ln r, \tag{6}$$

to properly simulate the scattering process.

With the information of the current position $\mathbf{r}_i$ and the wave vector $\hat{\mathbf{k}}$, the next scattering site $\mathbf{r}_f$ is given by

$$\mathbf{r}_f = \mathbf{r}_i + \tau \hat{\mathbf{k}}. \tag{7}$$

A check is made whether $\mathbf{r}_f$ is inside the scattering region. If $\mathbf{r}_f$ is inside the region, then $\mathbf{r}_f$ becomes the new initial position for next Thomson scattering. Otherwise the photon escapes from the region to reach an observer.

In the first case where $\mathbf{r}_f$ is inside the scattering region, we must choose the wave vector and polarization state of the photon. In our simulations, we adopt the density matrix formalism to produce the polarization and wave vector of the scattered photon (Lee et al. 1994). The density matrix associated with a given photon is represented by a 2×2 Hermitian matrix

$$\rho = \begin{pmatrix} \rho_{11} & \rho_{12} \\ \rho_{21} & \rho_{22} \end{pmatrix}, \tag{8}$$

where the 4 independent components of the photon density matrix are related to the Stokes parameters I, Q, U and V by

$$\rho_{11} = I + Q, \quad \rho_{22} = I - Q, \quad \rho_{12} = \rho_{21}^* = U + iV \tag{9}$$

(e.g., see Seon et al. 2022).

The Thomson scattering does not introduce circular polarization when the incident radiation is not circularly polarized unless the magnetic field is present (Agol & Blaes 1996). In this work, no magnetic field assumed to be present in the scattering medium and $V = 0$ for the initial photons generated at the center. Therefore, V remains zero throughout the entire scattering process and the density matrix becomes a real

symmetric matrix. Furthermore, we also assume that the line emitting source is also completely unpolarized so that

$$\rho_{11} = \rho_{22} = 0.5, \quad \rho_{12} = \rho_{21} = 0. \tag{10}$$

When no consideration of the circular polarization is made, the density matrix ρ' of the scattered photon propagating in the new direction $\hat{\mathbf{k}} = (\sin\theta'\cos\phi', \sin\theta'\sin\phi', \cos\theta')$ is related to that of the incident radiation with the unit wave vector $\hat{\mathbf{k}} = (\sin\theta\cos\phi, \sin\theta\sin\phi, \cos\phi)$ as follows (e.g. Lee 1999; Seon et al. 2022).

$$\begin{aligned}
\rho'_{11} &= \cos^2\Delta\phi\,\rho_{11} - \cos\theta\sin 2\Delta\phi\,\rho_{12} \\
&\quad + \cos^2\theta\sin^2\Delta\phi\,\rho_{22} \\
\rho'_{12} &= \frac{1}{2}\cos\theta'\sin 2\Delta\phi\,\rho_{11} \\
&\quad + (\cos\theta\cos\theta'\cos 2\Delta\phi + \sin\theta\sin\theta'\cos\Delta\phi)\,\rho_{12} \\
&\quad - \cos\theta(\sin\theta\sin\theta'\sin\Delta\phi \\
&\quad + \frac{1}{2}\cos\theta\cos\theta'\sin 2\Delta\phi)\,\rho_{22} \\
\rho'_{22} &= \cos^2\theta'\sin^2\Delta\phi\,\rho_{11} + \cos\theta'(2\sin\theta\sin\theta'\sin\Delta\phi \\
&\quad + \cos\theta\cos\theta'\sin 2\Delta\phi)\,\rho_{12} \\
&\quad + (\cos\theta\cos\theta'\cos\Delta\phi + \sin\theta\sin\theta')^2\,\rho_{22}
\end{aligned} \tag{11}$$

Here, $\Delta\phi = \phi' - \phi$ is the difference of the azimuthal angles made by the incident and scattered photons. The azimuthal dependence only through the difference $\Delta\phi$ shows the cylindrical symmetry of the scattering process with respect to the direction of the incidence.

It turns out that the probability distribution of the new unit wave vector $\hat{\mathbf{k}}'$ is given by

$$P(\theta', \phi'; \theta, \phi) = N(\rho'_{11} + \rho'_{22}), \tag{12}$$

where N is the normalization constant. The choice of θ' and ϕ' can be easily implemented using the rejection method. With the new wave vector $\hat{\mathbf{k}}_f$, the new Doppler factor along the new propagation direction should be assigned in accordance with Equation (20). Here, the electron velocity is chosen from a random deviate with a Gaussian distribution. Finally, when the photon escapes from the region, the final frequency is recorded along its propagation direction.

2.2. Frequency Redistribution Function

In this section, we test our Monte Carlo code to produce the frequency redistribution function and compare it with that derived by Dirac (1925). In the test simulation, we introduce a monochromatic line emitting source at an arbitrary location. A line photon is subsequently incident on a free electron region that is described by the Maxwell-Boltzmann distribution with a temperature $T = 10^4$ K. Here, the photon is forced to be scattered only once and escape from the region without further interaction. We collect the singly Thomson scattered photon and measure its frequency along the propagation direction. This process is iterated sufficiently until the frequency redistribution appears smooth for appropriate comparison. Here, the

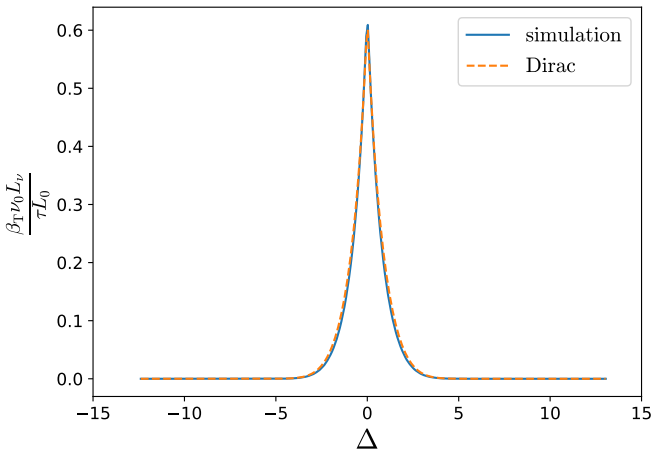

Figure 1. Distribution of the frequency shift introduced in an ensemble of singly Thomson-scattered photons. The dotted red line shows the frequency redistribution function introduced by Dirac (1925). The simulation data are shown by the solid blue line. In this simulation, all the photons are forced to be singly scattered and collected by the detector.

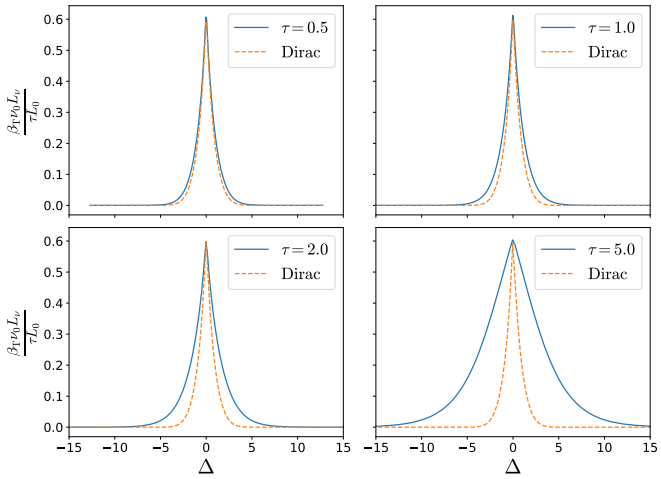

Figure 2. Line profiles of Thomson scattered photons in spherical regions from a monochromatic isotropic source at the center. The results of four values of $\tau_{\rm tot} = 0.5, 1, 2$, and 5 are shown.

frequency shift is measured using a dimensionless parameter Δ defined as

$$\Delta = \frac{\nu - \nu_0}{\beta_T \nu_0}, \quad \beta_T \equiv \left(\frac{2kT}{m_e c^2}\right)^{1/2}. \tag{13}$$

In Appendix A, we present the frequency redistribution function based on Dirac's approach in a heuristic manner (see also Loeb 1998; Mihalas 1978). In Figure 1, we show the distribution of frequency shift Δ from our collection of singly Thomson-scattered photons by the solid line. We also plot the frequency redistribution function given by Equation (33) with the dashed line. As is shown in the result, the agreement between our simulation and Dirac's redistribution function is excellent. The sharp peak at the center ($\Delta = 0$) is attributed to the monochromaticity of the emission line source. The full width at half maximum of the frequency redistribution function is measured to be $\sim 1.1\Delta$. About a half of singly scattered line

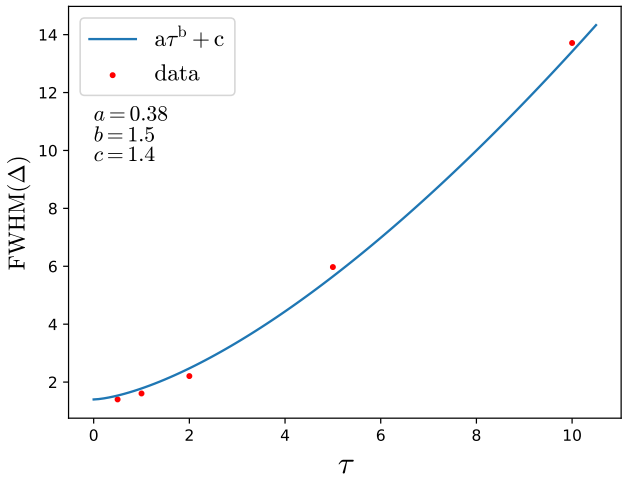

Figure 3. The full width at half maximum of the frequency redistribution function as a function of the total Thomson scattering optical depth $\tau_{\rm tot}$ in a spherical ionized region. The Monte Carlo data points are fitted using the function $f(\tau_{\rm tot}) = 0.38\tau_{\rm tot}^{3/2} + 1.4$, which is shown by the solid blue line.

photons reside in the interval $(-0.5\Delta, +0.5\Delta)$.

In Figure 2, we show our simulation results obtained for 4 values of $\tau_{\rm tot}$ in the range between 0.5 and 5. The scattering region is a sphere of uniform electron density. The horizontal axis is the dimensionless frequency deviation Δ. In the upper left panel, we show our result for $\tau_{\rm tot} = 0.5$, in which case most photons are singly scattered and only a very small percentage of photons are scattered doubly or more. Therefore, the line profile should be closely approximated by the frequency redistribution function given by Dirac (1925).

A notable deviation is seen as $\tau_{\rm tot}$ exceeds unity. It appears that the line profiles retain similarity and simply the line width increases as $\tau_{\rm tot}$ increases. One should also note that as $\tau_{\rm tot}$ increases, the total line flux of Thomson scattered radiation also increases. For $\tau_{\rm tot} > 2$ almost all the photons are scattered so that they escape from the region by diffusion in real space while they undergo diffusion in frequency space at the same time.

In Figure 3, we show the full width of the Thomson line profiles shown in Figure 2 to focus on the effect of the frequency diffusion as a function of the total Thomson scattering optical depth $\tau_{\rm tot}$. As is naturally expected, the wing broadening is monotonically increasing as a function of $\tau_{\rm tot}$. The Monte Carlo data points are fitted using the functional form

$$f(\tau_{\rm tot}) = a\tau_{\rm tot}^b + c, \tag{14}$$

where the fit parameters are obtained as

$$a = 0.38, \quad b = 1.5, \quad c = 1.4. \tag{15}$$

The fitting curve is shown by the blue solid line in Figure 3.

3. Thomson Scattering in Spherical Regions

3.1. Surface Brightness

As a first step, we investigate the spatial diffusion process of Thomson-scattered radiation in spherical ionized regions. Even though we expect the polarization pattern along the circumference, we focus on the surface brightness in the spherical geometries in this section. In Figure 4, we show the surface brightness of spherical free electron regions, where a point-like monochromatic emission source is embedded at the center. The spherical region is assumed to be of uniform density and the physical dimension is given by the Thomson scattering optical depth $\tau_{\rm Th}$ measured along the radial direction from the center. Each image is produced with a total of 10^8 photons from our Monte Carlo simulations.

In the figure, the simulation results for $\tau_{\rm Th} = 0.1, 1, 5,$ and 10 are shown. In order to better understand the diffusion process in phase space, we divide the line photons into core and wing photons. The core photons are defined as those with frequency ν satisfying the following relation

$$\left|\frac{\nu - \nu_0}{\nu_0}\right| \leq \frac{v_{\rm th}}{c}. \tag{16}$$

The right panels show the surface brightness integrated over the entire frequency range. Because the Thomson scattering cross section is wavelength independent, the photon distributions shown by the surface brightness correspond to the well-known random-walk processes. For $\tau_{\rm Th} \leq 1$, the central emission source is clearly seen, whereas the central source is virtually indiscernible for $\tau_{\rm Th} = 10$.

The left and middle panels of Figure 4 show the surface brightness of the same spherical regions using the core and wing photons, respectively. In the cases of $\tau_{\rm Th} = 0.1$ and 1.0, the surface brightness of core photons is similar to that of wing photons. In particular, the center is quite bright for both core and wing surface brightness images. The wing photons from the center pixel are those photons that are backward-scattered with approaching or receding electrons. More specifically, if a line center photon emitted in the opposite direction to the line of sight is incident on an electron approaching the center and gets scattered toward the observer, the scattered photon acquires a negative Doppler factor that tends to be less than $-v_{\rm th}/c$ and become a blue wing photon. Similarly, a backward scattering with a receding electron tends to yield a red wing photon.

However, a backward scattering with an electron with a negligible Doppler factor results in a core photon. In addition, no frequency change is made from a forward scattering. Therefore, the center pixel in the core surface brightness image is made up of the non-scattered line center photons, forward scattered photons and those photons scattered backward with electrons with negligible Doppler factors.

Figure 5 shows the number $N_{\rm photon}$ of photons in pixels lying on the horizontal diameter of the circular image shown in Figure 4. The blue lines show the core photon distributions including non-scattered line center photons. The orange lines show the distributions of wing photons, and the gray dashed lines indicate the distributions of all the photons.

In this figure, the decrease of the center dominance is clearly seen as $\tau_{\rm Th}$ increases. In the case of $\tau_{\rm Th} = 0.1$, we find that the core and wing photons are distributed in a similar way except at the center region. The region outside

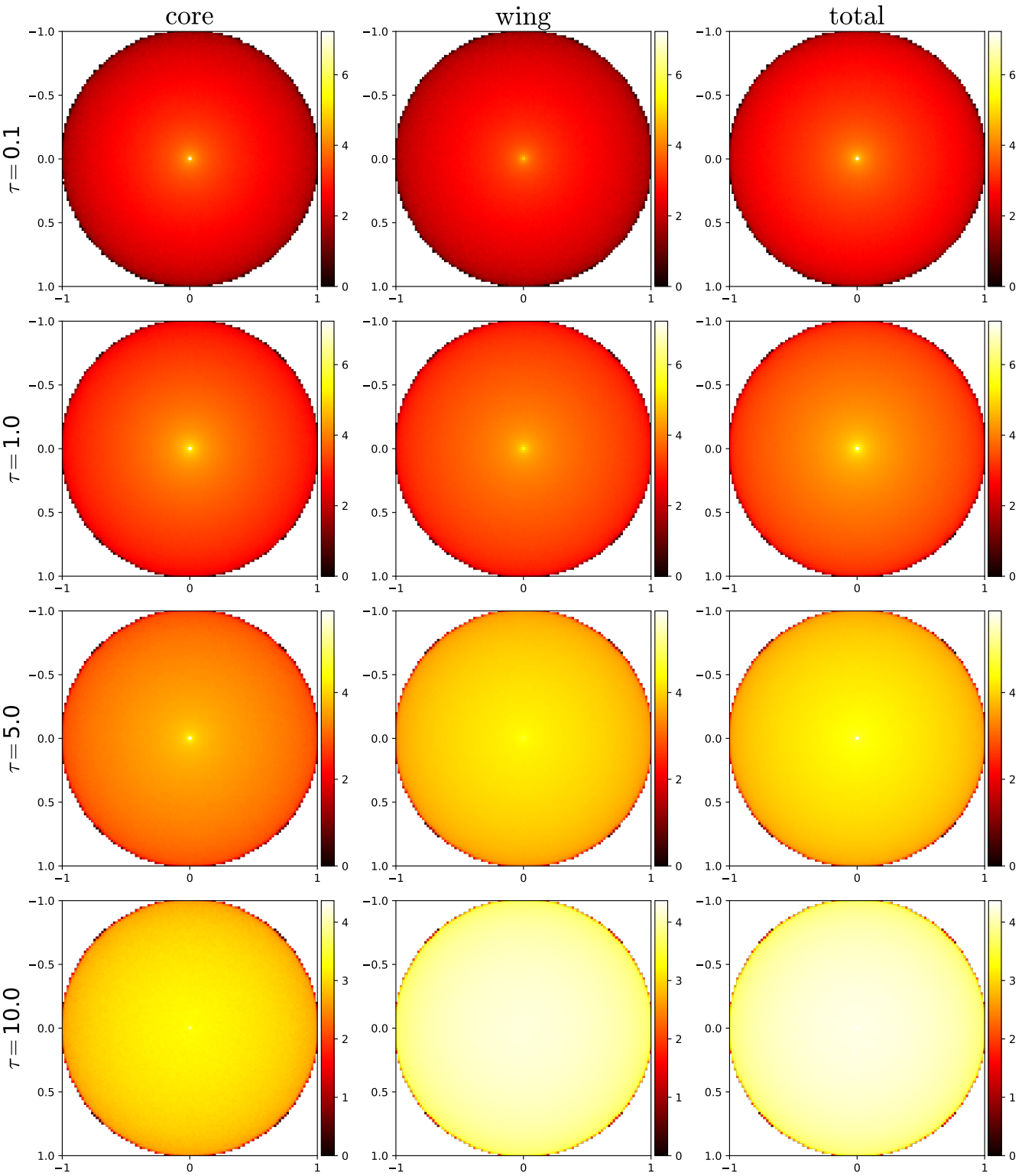

Figure 4. Surface brightness of Thomson-scattered line radiation in spherical ionized regions with Thomson optical depths $\tau_{\rm Th} = 0.1, 1, 5,$ and 10. The emission line source is monochromatic and point-like embedded at the center. The line photons are divided into the core and wing photons, where the core photons satisfy the condition given by Equation (16).

the center is filled with singly Thomson-scattered photons and local variation of the spectral distribution is expected to be negligible due to the wavelength independence of the Thomson scattering cross section.

When $\tau_{\rm Th}$ increases, the spatial diffusion is significant, which enhances surface brightness as $r/r_{\rm max}$ increases. The spatial diffusion is also tightly connected to diffusion in frequency space so that the number of core photons decreases considerably as $\tau_{\rm Th}$ exceeds unity. In particular, for $\tau_{\rm Th} = 10$, the number of core photons is smaller than that of wing photons by an order of magnitude.

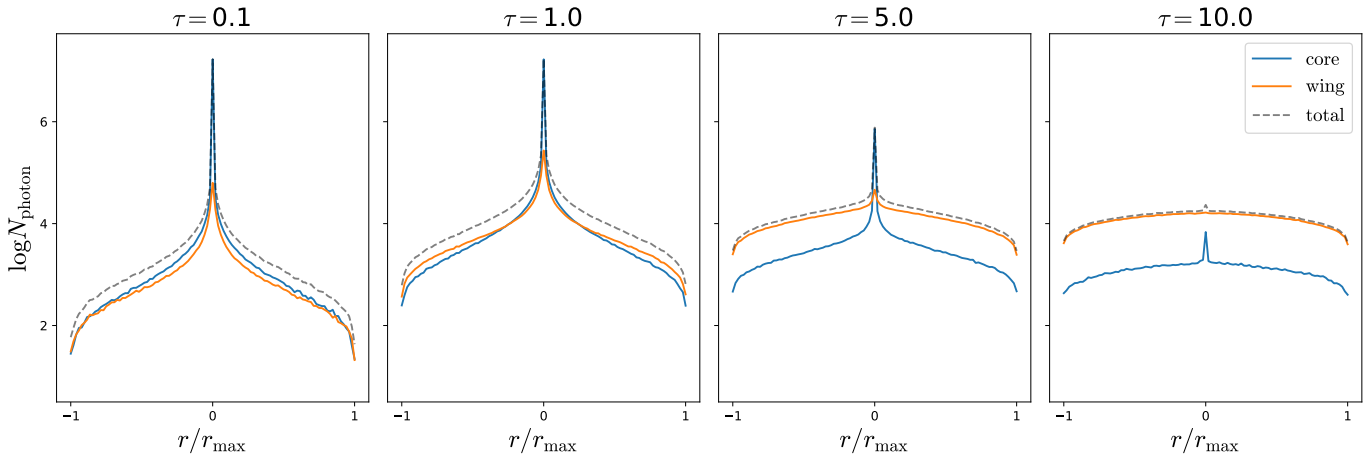

Figure 5. Surface brightness of Thomson-scattered line radiation in the same spherical ionized regions considered in Figure 4. The blue and orange lines show the surface brightness of the core and wing photons, respectively. The surface brightness profiles of the entire line photons are shown by the dashed line. As $\tau_{\rm Th}$ becomes larger than 5, most of emergent line photons are wing photons through the diffusion in real and frequency spaces.

3.2. Profile Broadening in Phase Space

In Figure 6, we show the locally varying profiles of Thomson-scattered emission line emergent from the same spherical free electron regions considered in Figures 4 and 5. The blue, orange, green, red and purple lines show the profiles at the circular rings with the normalized radii $r = 0.05, 0.25, 0.45, 0.65,$ and 0.85 from the center of the circular image. The profiles are normalized by requiring the peak value equal to unity. In all the cases, the profile width increases as a function of τ. Even in the low Thomson optical depth of $\tau_{\rm Th} = 0.5$, the profiles get broadened toward the boundary despite the dominance of singly Thomson-scattered photons.

In the case of $\tau_{\rm Th} = 10$, all the profiles are similar and the full width at half maximum is $\sim 20\, v_{\rm th}$, which is quite significant. In this thick geometry, diffusion both in real and frequency spaces is almost complete. This is also confirmed from the images shown in Figure 4, where the center pixel is inconspicuous for $\tau_{\rm Th} = 10$. In contrast, for $\tau_{\rm Th} \leq 5$, the profile widths near the image center (shown by the blue lines) are significantly narrower than those near the edge (shown by the purple lines). This is because the memory of initial forward scattering is not completely erased, which is also confirmed by the bright center pixel in Figure 4.

4. Polarization Development in Slab Regions

In this section, we focus on the polarization development of Thomson-scattered radiation in slab regions. As in the previous sections, we consider a monochromatic point source, which is embedded at the center of the slab. For the sake of simplicity, the slab is also assumed to be of uniform electron density and characterized by the vertical Thomson scattering optical depth $\tau_{\rm Th}$. Here, the Thomson scattering optical depth $\tau_{\rm Th}$ is measured along the slab normal direction from the center. Our slab model is a pill box with the diameter being 5 times larger than the thickness, and we collect photons only emerging through the cylinder top. As long as $\tau_{\rm Th} \geq 1$, a negligible fraction of photons escape through the lateral side so that the pill box can be effectively regarded as an infinite slab.

In Figure 7, we reproduce a representative result obtained by Phillips & Meszaros (1986), in which the photon source is located on the midplane of the slab. The vertical axis shows the (signed) degree of linear polarization, where the negative and positive degrees of polarization represent polarization developed in the direction parallel and perpendicular to the slab normal, respectively. When the slab has a small Thomson optical depth, the linear polarization is dominated by singly scattered line photons, which are strongly polarized in the normal direction to the slab.

As we increase the slab optical depth to $\tau_{\rm Th} = 10$, the linear degree of polarization approaches that obtained by Chandrasekhar (1960), which is marked by the stars in the figure. The agreement is excellent, which serves as a check of the code. In the grazing direction $\mu = 0$ the polarization flip occurs when $\tau_{\rm Th} = 1$.

In Figure 8, we show the surface brightness of the free electron slabs with the vertical Thomson optical depth taking the value of $\tau_{\rm Th} = 1, 2, 5,$ and 10, when the line of sight makes an angle of 80° with the slab normal. The left panel shows the surface brightness of the Stokes parameter I. The surface brightness for Q and U are displayed in the second and third panels, respectively. The right panels show the linear degree of polarization. The images shown in Figure 8 are prepared in such a way that the line of sight passing the emission source meets the origin of the coordinate system, resulting in the top surface of the pill box appearing as an ellipse with the center lying on the positive $y-$axis.

In the case of $\tau_{\rm Th} = 1$, the Stokes Q is strong positive near the region of the strongest Stokes I, whereas we have strong negative Q at side regions. In contrast, the Stokes U is strong positive at the region left of the center and strong negative on the opposite side. Due to the symmetry of the scattering geometry, the polarization direction of the total ra-

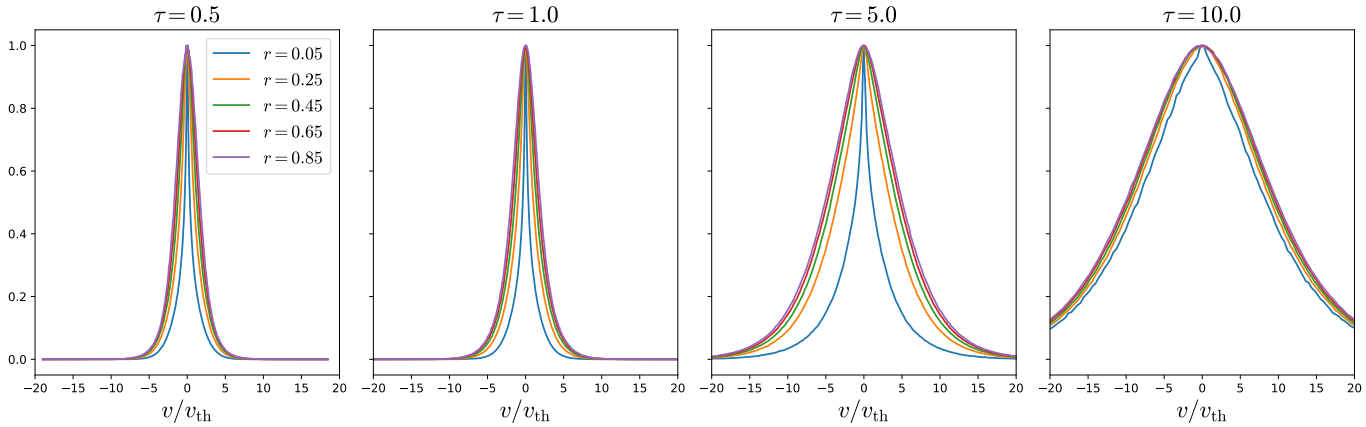

Figure 6. Locally varying profile broadening of Thomson-scattered line radiation in spherical regions with the radial Thomson optical depths $\tau_{\rm Th} = 0.5, 1, 5$, and 10. The blue, orange, green, red and purple lines show the profiles at the circular rings with the normalized radii $r = 0.05, 0.25, 0.45, 0.65$, and 0.85 from the center of the circular image.

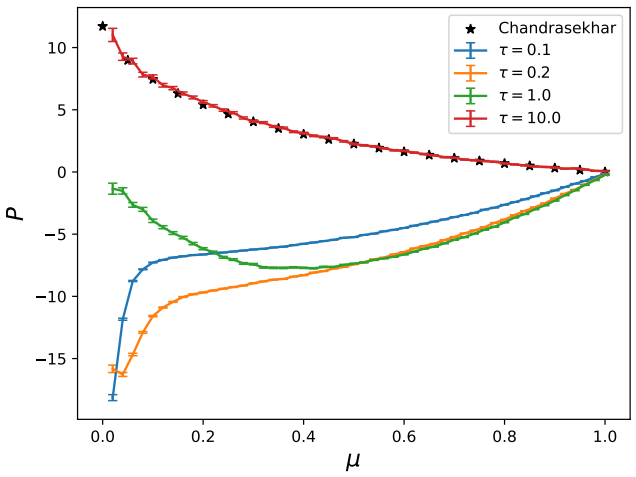

Figure 7. Linear degree of polarization of Thomson scattered radiation from ionized slabs of uniform electron density obtained by Phillips & Meszaros (1986) and reproduced from our simulation. The color lines show the results by Phillips & Meszaros (1986) and our simulation data are marked with error bars. The emission source is embedded uniformly on the midplane of the slab. The stars show the linear degree of polarization presented by Chandrasekhar (1960) for extremely Thomson optically thick slab.

diation integrated over all the slab surface should be either parallel or perpendicular to the slab normal. This implies that the sum of the Stokes U over the entire slab surface vanishes in all the cases and the total linear degree of polarization is determined by the total sum of Q with respect to I (e.g., Lee et al. 1994; Schmid 1995).

In order to trace the polarization flip represented by the sign change of Q from negative to positive as $\tau_{\rm Th}$ increases, we need to pay attention to the Q surface brightness. As is seen in Figure 8, we notice that positive Q persists near the center for all $\tau_{\rm Th}$. However, the regions left and right to the center are dominated by strong negative and positive U, respectively, when $\tau_{\rm Th}$ is small and get negligible as $\tau_{\rm Th}$ increases. From this result, we may conclude that the polarization flip is attributed to the robustness of Q near the center region while the other regions become very weak in Q. A very similar behavior has been discussed for the transfer of Lyα in a very thick neutral medium, because the phase function of Thomson scattering is shared by Rayleigh scattering (Chang et al. 2017).

5. Summary and Discussion

We have carried out Monte Carlo simulations of the diffusion process of Thomson-scattered line photons in phase space. For simplicity, a point-like monochromatic line source is chosen. The scattering geometry is either spherical or slab-like, where the emission source is located at the center. In particular, we have investigated the polarization flip from the slab normal direction to the slab plane direction that takes place in slab geometries as the Thomson optical depth increases. We find that the polarization near the center region persists to be along the slab plane while the remaining regions are negligibly polarized as $\tau_{\rm Th}$ increases.

It is interesting to note that Hα emission lines of most symbiotic stars and some planetary nebulae exhibit prominent broad wings. The broad Hα wings are proposed to be formed in the fast and tenuous wind from the hot white dwarf star. According to Nussbaumer et al. (1989), Raman scattering of continuum near Lyβ may also be responsible for the formation of broad Hα wing features (see also Schmid 1989; Chang et al. 2018; Lee 2000). If Raman scattering with atomic hydrogen is responsible for broad Balmer wings, then the Balmer wings appear stronger in neutral regions than in ionized regions. Deep high resolution spectroscopy covering Hα and Hβ will shed much light on the origin of these wing features.

On the other hand, *FUSE* and *IUE* spectra of these objects also reveal broad wing features around many UV emission lines that appear to be consistent with Thomson scattering with free electrons in the emission line region. In particular, Sekeráš & Skopal (2012) performed line fitting analyses to UV emission lines with well-developed wings to infer the Thomson optical depth in several symbiotic stars. With the availability of integrated field spectrographs, the local variation of wing strengths may provide crucial information pointing out the

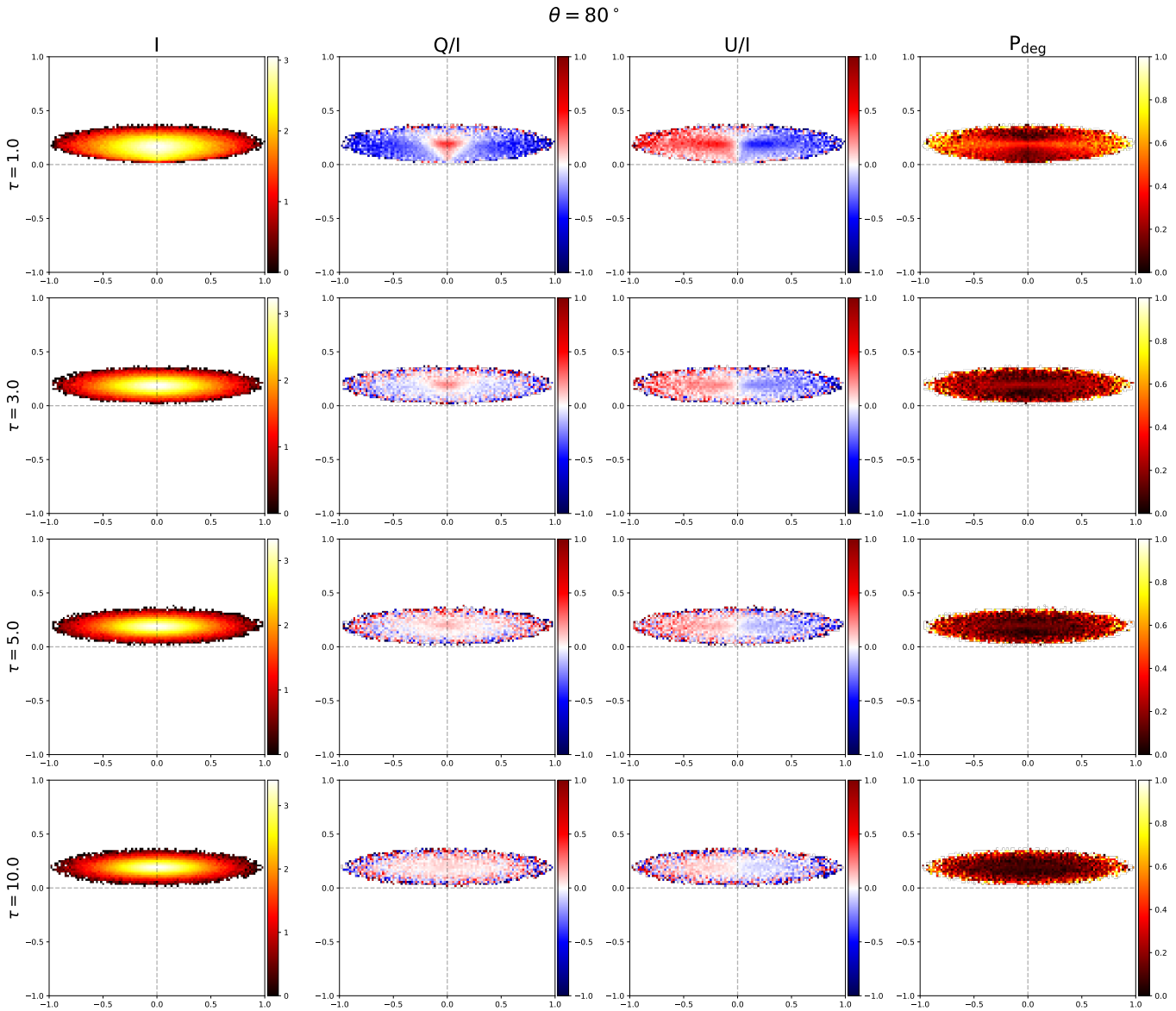

Figure 8. Surface brightness and polarization of Thomson-scattered radiation emergent from a slab making an angle of 80° with the slab normal. The monochromatic and point-like line source is embedded at the center of the slab. The first, second and third panels from the left show the surface brightness of the Stokes parameters I, Q and U, and the right panels show the linear degree of polarization.

contributions of Raman and Thomson scattering processes to the wing formation.

The diffusion process in phase space of Thomson-scattered line photons can be an important reference frame against which similar radiative processes can be compared. For example, in an extremely thick neutral region, Lyα photons are transferred through diffusion in frequency and real spaces in a more complicated way than Thomson-scattered line photons. Extremely thick neutral regions can be found in the intergalactic medium at around the end of the cosmic reionization era, where Lyα photons are scattered so many times before escape and may be observed as a Lyα halo spread significantly both in real and frequency spaces (e.g., Park et al. 2022).

A similar environment is found in Lyman alpha blobs, where substantially extended Lyα emission is observed. Chang et al. (2023) propose that Lyα photons emitted from an active galactic nucleus may spread through the circumgalactic medium accompanied by profile broadening and polarization development (e.g., Kim et al. 2020). The surface brightness and local variation of polarization may provide crucial information regarding the distribution and kinematics of the scattering material.

Acknowledgments

The authors are very grateful to Seok-Jun Chang for helpful comments. We are also grateful to the referee, who provided constructive comments. This research was supported by the National Research Foundation of Korea (NRF) grants funded by the Korea government (No. 2018R1D1A1B07043944).

Appendix A. Frequency Redistribution of Thomson-scattered Radiation

In this appendix, we discuss the frequency redistribution for Thomson scattering. An incident photon with a definite frequency ν is Thomson-scattered in an ionized region with a fast moving electron to propagate in another direction with a frequency ν' which differs from ν. By the frequency redistribution function, we mean the assignment of a new frequency acquired by the scattered photon as a function of the incident photon frequency. The frequency redistribution function should be dependent on the velocity distribution of the free electrons in the scattering medium. Dirac (1925) presented the frequency redistribution function in a scattering medium, which is in a thermal distribution with a temperature T. Here, we summarize the Dirac's approach, which will be compared with our Monte Carlo simulation results.

According to Dirac (1925), the frequency redistribution function in an ionized region described by the Maxwell-Boltzmann distribution with temperature T is given by

$$R(\nu', \hat{\mathbf{n}}'; \nu, \hat{\mathbf{n}}) = \frac{3}{4}\frac{(1+\mu^2)}{\sqrt{2\pi(1-\mu)}\beta_T\nu}\exp\left[-\frac{(\nu-\nu')^2}{2\beta_T^2(1-\mu)\nu^2}\right], \quad (17)$$

where $\mu = \hat{\mathbf{n}}\cdot\hat{\mathbf{n}}'$ is the cosine of the angle θ subtended by the propagation directions of the incident and the scattered radiation. The dimensionless parameter β_T is defined as

$$\beta_T = \left(\frac{2kT}{m_e c^2}\right)^{1/2}, \quad (18)$$

which stands for the temperature scale relative to the electron rest mass energy (e.g., Loeb 1998; Mihalas 1978). When the parameter β_T is comparable to unity, then the photon momenta are big enough to disturb the electron momentum quite significantly. Therefore, the special relativistic effects are not negligible any more and the scattering process should be treated as the Compton scattering process.

Here, the Boltzmann factor $e^{-mv^2/(2kT)}$ is associated with the Doppler factor acquired by the scattered photon, which may be written as

$$\frac{(\nu'-\nu)}{\nu} = \frac{\mathbf{v}}{c}\cdot(\hat{\mathbf{n}}'-\hat{\mathbf{n}}). \quad (19)$$

Noting that the Maxwell-Boltzmann distribution is isotropic, we may consider that the electron velocity is along the direction $\hat{\mathbf{n}}'$ without losing generality. Hence, we may write

$$\frac{(\nu'-\nu)}{\nu} = \frac{v}{c}(1-\mu), \quad (20)$$

or equivalently

$$v = c\left[\frac{(\nu'-\nu)}{\nu(1-\mu)}\right], \quad (21)$$

From this relation, one may find that the number density of electrons contributing to the Doppler factor of $(\nu'-\nu)/\nu$ making a scattering angle of $\theta = \cos^{-1}\mu$ is proportional to the Boltzmann factor given by

$$\exp\left[-\frac{m_e}{2kT}\left\{\frac{c(\nu'-\nu)}{\nu(1-\mu)}\right\}^2\right] = \exp\left[-\frac{(\nu-\nu')^2}{2\beta_T^2(1-\mu)\nu^2}\right]. \quad (22)$$

The normalization constant for this Boltzmann factor is $\sqrt{2\pi\beta_T^2(1-\mu)\nu^2}$, which justifies Equation (17).

We are also interested in the angle averaged of the frequency redistribution function in order to obtain the kernel function, which provides the frequency distribution of the scattered radiation for a monochromatic line radiation source. Fixing the the frequency of the incident radiation $\nu = \nu_0$, we consider

$$R(\nu', \nu) = \int d\nu \int \frac{d\Omega}{4\pi}\int\frac{d\Omega'}{4\pi}R(\nu', \hat{\mathbf{n}}'; \nu, \hat{\mathbf{n}})\delta(\nu-\nu_0). \quad (23)$$

Taking advantage of the isotropy of the Maxwell-Boltzmann distribution, and in the classical regime of $\beta_T \ll 1$, in which $\nu'-\nu \ll \nu$, one may realize that the relevant integral to be taken care of is given by

$$\int_{-1}^{1} d\mu\,\frac{1+\mu^2}{\sqrt{1-\mu}}\exp\left[-\frac{1}{2}\frac{\Delta^2}{(1-\mu)}\right]. \quad (24)$$

This integral admits a much simplified expression in terms of the complementary error function defined as $\mathrm{erfc}(x) \equiv (2/\sqrt{\pi})\int_x^\infty \exp(-t^2)dt$. Explicitly, we perform integration of the following expression

$$\begin{aligned}\beta_T\nu_0 R(\nu', \nu) &= \beta_T\nu_0\int_{-1}^{1}\frac{d\mu}{2}R(\nu_0, \nu, \mu)\\ &= \frac{3}{8\sqrt{2\pi}}\int_{-1}^{1}d\mu\,\frac{1+\mu^2}{\sqrt{1-\mu}}\exp\left[-\frac{\Delta^2}{2(1-\mu)}\right].\end{aligned} \quad (25)$$

Using substitution of $\frac{\Delta^2}{2(1-\mu)} = x^2$, one may realize the relevant integral becomes

$$A(\Delta) = \frac{3|\Delta|}{8\sqrt{\pi}}\int_{\frac{|\Delta|}{2}}^{\infty}dx\left(\frac{2}{x^2}-\frac{\Delta^2}{x^4}+\frac{\Delta^4}{4x^6}\right)e^{-x^2}. \quad (26)$$

Integrating by parts, for a positive constant a, we note that

$$\int_a^\infty x^{-2}e^{-x^2}dx = \frac{1}{a}e^{-a^2} - \sqrt{\pi}\,\mathrm{erfc(a)}. \quad (27)$$

For an even natural number $2n$, if we define

$$I_n = \int_a^\infty x^{-2n}e^{-x^2}dx, \quad (28)$$

then integration by parts yields a following recurrence relation

$$I_n = \frac{1}{2n-1}\frac{e^{-a^2}}{a^{2n-1}} - \frac{2}{2n-1}I_{n-1}. \quad (29)$$

Here, it is also noted that

$$I_0 = \frac{\sqrt{\pi}}{2}\mathrm{erfc}(a). \quad (30)$$

For $n = 2$, we obtain

$$I_2 = \frac{1-2a^2}{3^3}e^{-a^2} + \frac{2\sqrt{\pi}}{3}\mathrm{erfc}(a). \quad (31)$$

Also for $n = 3$,

$$I_3 = \frac{3-2a^2+4a^4}{15a^5}e^{-a^2} - \frac{4\sqrt{\pi}}{15}\mathrm{erfc}(a). \quad (32)$$

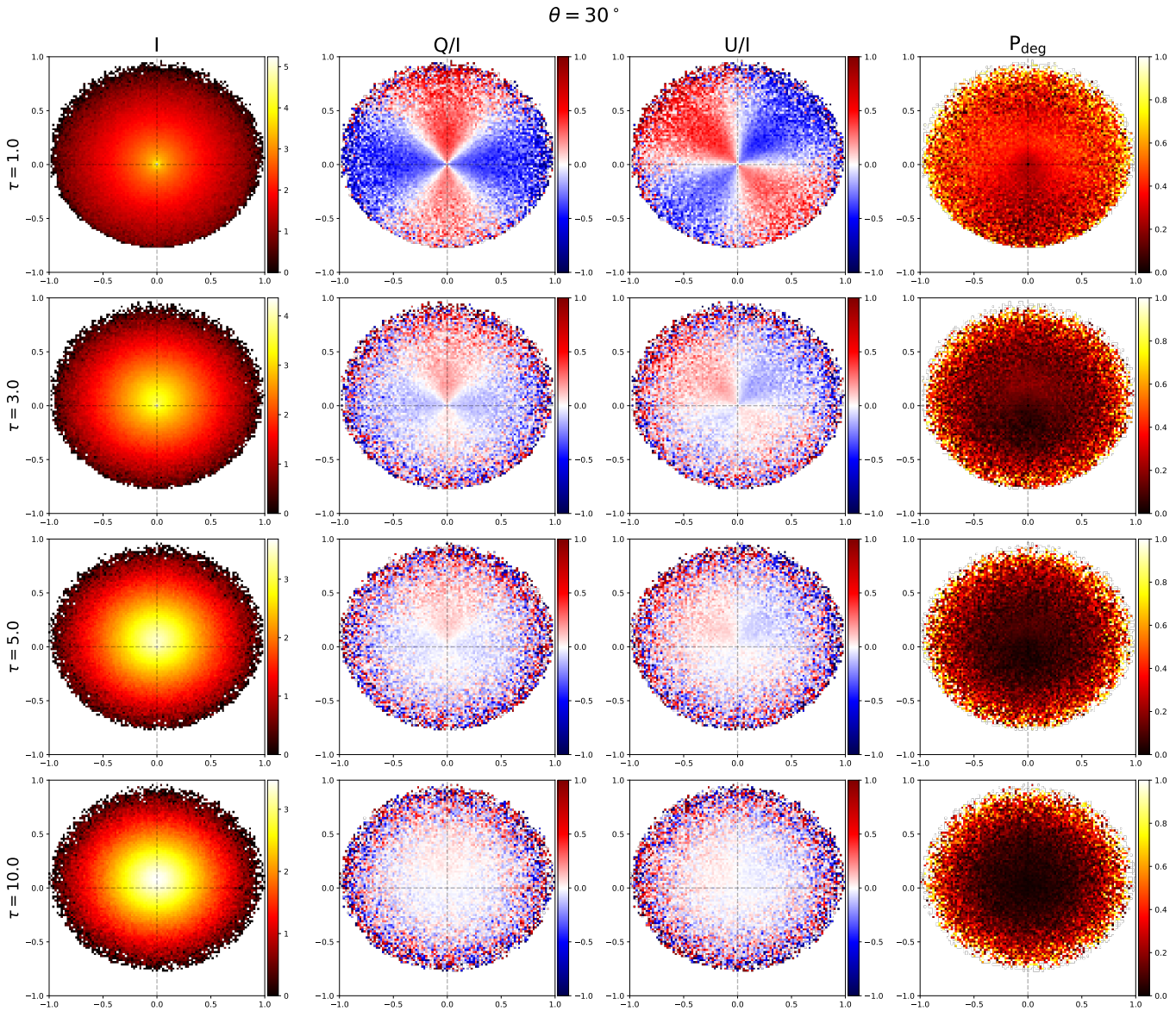

Figure 9. Surface brightness and polarization of Thomson-scattered line radiation emergent from a slab making an angle of 30° with the slab normal. The other parameters are the same as those of Figure 8.

Using these results, we finally obtain the frequency redistribution function written as

$$R(\nu',\nu) = (\beta_T \nu_0)^{-1} \left[\left(\frac{11}{10} + \frac{2}{5}\Delta^2 + \frac{\Delta^4}{20} \right) \frac{e^{-\Delta^2/4}}{\sqrt{\pi}} - \left(\frac{3}{2} + \frac{\Delta^2}{2} + \frac{\Delta^4}{20} \right) \frac{|\Delta|}{2} \mathrm{erfc}\left(\frac{|\Delta|}{2} \right) \right]. \quad (33)$$

Appendix B. Polarization Distribution of Thomson-scattered Radiation in Slab Geometry

For illustrative purpose, in Figure 9, we show the polarization and surface brightness of Thomson-scattered line radiation that emerge to the line of sight making an angle of 30° with the slab normal. When $\tau_{\rm Th}$ is smaller or equal to unity, the polarization parallel to the slab normal is dominant, as is shown by the blue dots in the Q/I images. When $\tau_{\rm Th}$ exceeds 5, the polarization in the parallel direction weakens, while the polarization in the perpendicular direction persists. As Chandrasekhar (1960) showed, the overall polarization is weaker for radiation emerging with $\theta = 30°$ than that with $\theta = 80°$ shown in Figure 8.

It is interesting to note that when $\tau_{\rm Th}$ is low, we find that the regions below the image center is particularly weakly polarized. The weak polarization may be explained by considering that the location on the slab surface where the observer's line of sight hit should be dominated by forward-scattered radiation. However, as $\tau_{\rm Th}$ increases, the diffusion in real and frequency spaces tends to erase the memory of the initial starting position.

References

Afanasiev, V. L., Popović, L. Č., & Shapovalova, A. I. 2019, MNRAS, 482, 4985

Agol, E., & Blaes, O. 1996, MNRAS, 282, 965

Angel, J. R. P. 1969, ApJ, 158, 219

Chandrasekhar, S. 1960, Radiative transfer (New York: Dover Publications)
Chang, S.-J., Lee, H.-W., Lee, H.-G., et al. 2018, ApJ, 866, 129
Chang, S.-J., Lee, H.-W., & Yang, Y. 2017, MNRAS, 464, 5018
Chang, S.-J., Yang, Y., Seon, K.-I., Zabludoff, A., & Lee, H.-W. 2023, ApJ, 945, 100
Dirac, P. A. M. 1925, MNRAS, 85, 825
Kim, E., Yang, Y., Zabludoff, A., et al. 2020, ApJ, 894, 33
Kim, H. J., Lee, H.-W., & Kang, S. 2007, MNRAS, 374, 187
Lee, H.-W. 1999, ApJ, 511, L13
Lee, H.-W. 2000, ApJ, 541, L25
Lee, H. W., Blandford, R. D., & Western, L. 1994, MNRAS, 267, 303
Loeb, A. 1998, ApJ, 508, L115
Mihalas, D. 1978, Stellar atmospheres (San Francisco: W. H. Freeman & Company)
Nussbaumer, H., Schmid, H. M., & Vogel, M. 1989, A&A, 211, L27
Osterbrock, D. E. 1989, Astrophysics of gaseous nebulae and active galactic nuclei (Sausalito, Calif.: University Science Books)
Park, H., Kim, H. J., Ahn, K., et al. 2022, ApJ, 931, 126
Phillips, K. C., & Meszaros, P. 1986, ApJ, 310, 284
Schmid, H. M. 1989, A&A, 211, L31
Schmid, H. M. 1995, MNRAS, 275, 227
Sekeráš, M., & Skopal, A. 2012, MNRAS, 427, 979
Seon, K.-I., Song, H., & Chang, S.-J. 2022, ApJS, 259, 3
Warner, B. 1995, Cambridge Astrophysics, Vol. 28, Cataclysmic variable stars (Cambridge University Press)